Adaptive Signal Processing Laboratory (ASPL)
Electrical and Computer Engineering Department
University of Florida

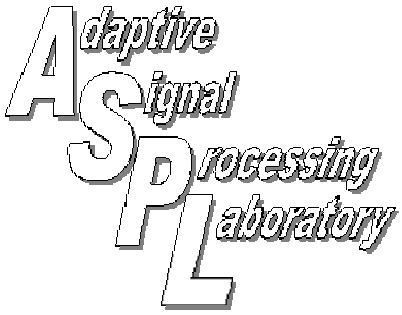

Progress on numerical modeling of the UF airborne low SNR lidar

ASPL Report No. Rep_2008-02-001

Tristan Cossio, K.C. Slatton, W.E. Carter

February 18, 2008

Point of Contact:
Prof. K. C. Slatton
University of Florida; PO Box 116130; Gainesville, FL 32611
Tel: 352.392.0634, Fax: 352.392.0044, E-mail: slatton@ece.ufl.edu

Progress on numerical modeling of the UF airborne low SNR lidar

Tristan Cossio[1], K.C. Slatton[1,2], W.E. Carter[2]
1: Department of Electrical and Computer Engineering
2: Department of Civil and Coastal Engineering
University of Florida; PO Box 116130; Gainesville, FL 32611
Tel: 352.392.0634, Fax: 352.392.0044,
E-mail: {tcossio@ecel.ufl.edu}, {slatton@ece.ufl.edu}

<This was an annual report for Cossio's NASA GSRP Fellowship>

1) Introduction

Commercially marketed airborne laser swath mapping (ALSM) instruments, also known as laser altimeters or lidar sensors, currently use lasers with sufficient energy per pulse (typically about 100 micro-joules) in combination with optics of sufficient aperture, to obtain return signals of thousands of photons per shot [Slatton, *et al*., 2005]. Strong returns make it possible to achieve a high signal-to-noise ratio (SNR) using standard noise suppression techniques, such as temporal (range gate), spatial (field stop) and spectral (narrow band-pass optical) filters. However, to keep the peak power levels low enough to avoid damaging optical components and comply with eye-safety regulations, the laser pulse lengths are typically about 10 nanoseconds, which is equivalent to about 3 meters of range. To achieve a range resolution of a few centimeters, the round trip travel time of the laser pulse must be measured to about one percent of the pulse length - a challenge when the return pulses vary in amplitude by 2 to 3 orders of magnitude and the shapes of many are distorted by reflection from rough uneven surfaces.

The high pulse power (and relatively low pulse frequency for space based lidar) approach typically used in modern systems favors a high SNR over other aspects of the system, including weight, size, and power consumption. As such, low SNR (LSNR) lidar can be viewed as an alternative to traditional ALSM methods. LSNR systems are based on emitting a train of much lower energy pulses. Previous LSNR-ALSM projects include MIT Lincoln Laboratory's Jigsaw sensor, the RULLI system developed by Los Alamos National Laboratory (LANL), and prototype sensors developed at NASA's Goddard Space Flight Center (GSFC). However, the defense-related applications (of the Lincoln Labs and LANL systems) and the high cost of custom sensor components limited the wide-spread application of these systems. The recent release of commercially available, highly sensitive photo-multiplier tubes (PMTs) and fast electronics for data capture has opened up LSNR-ALSM to a larger set of developers and users, including the University of Florida (UF), which has worked on the development of a LSNR lidar known as the Coastal Area Tactical-mapping System (CATS).

My efforts have been focused on the development of a LSNR lidar system simulator and preliminary analysis of simulated data. While parameters in the simulator have been specified for UF's CATS system, which is due for final testing in early 2008, the code has been left flexible to allow for performance analysis on a variety of systems. The intent is that this research can eventually be made relevant to ongoing NASA activities in LSNR lidar by providing a tool to explore the design trade space of potential LSNR lidar system configurations. The CATS

system has been designed as a low-altitude, low-power system that provides contiguous ground coverage (no gaps between footprints) with a spatial (horizontal) resolution of a few decimeters. Designed to use a frequency-doubled Nd:YaG laser operating at 532 nm, the system is intended for high resolution mapping of the coastal zone. The CATS laser pulse rate is relatively low (about 8 kHz) so that contiguous ground coverage and spatial resolution are achieved by splitting the outgoing beam into an array of 96 beamlets with nominally equal power in each beamlet via a holographic element [Carter, *et al*., 2004; Slatton, *et al*., 2005].

The objective of this work is to calculate system outputs based on ideal circumstances (true values for plane attitude, position, scanner angle, etc.) and evaluate performance as a function of system characteristics and environmental conditions. Additionally, noise and interpolation errors can be introduced into the multirate signals and the resulting effects on projected ground points and probability of detection can be quantified. All coding has been done in Matlab. Any future coding will also be done in Matlab to facilitate rapid algorithm development, easy visualization, and code sharing among Dr. Slatton's students. However, I do have experience in IDL and C/C++ and can work with those languages as needed.

2) Current Work

Previous reports have detailed the geometrical-optical approach to range acquisition and the algorithms for estimating signal strength and noise levels. These components have been integrated into a single fully functioning numerical model as described in my poster presented at the fall 2007 GSRP workshop. Details of this complete process have been presented to Dr. Harding and GSFC personnel, and are available upon request.

At the suggestion of GSFC personnel, further investigation into the effects of laser phenomenology on the expected return pulse has been completed. Major changes to the simulator's bathymetric algorithms are detailed in this report. Additionally, preliminary analysis of simulator results has been completed. Sample performance measurements for topographic and bathymetric simulations are presented. The basic algorithm for determining mean sea surface height and correcting for index-of-refraction effects is discussed. Future plans, including evaluation of target detection performance and implementation of an improved vegetation model, are described in the final section.

a) Laser Phenomena

A number of phenomena contribute to fluctuation in the expected laser irradiance. Although speckle and scintillation were initially dismissed as contributing negligible modulation to the return waveform, the validity of this assumption was brought into question by GSFC personnel. Here, we investigate in more detail each phenomenon's expected impact on the return waveform of LSNR ALSM systems.

Laser speckle causes random modulation in the observed waveform of highly coherent light. The measured intensity at the receiver can be considered an integrated version of a point-intensity speckle pattern [Goodman, 1975]. The essential quantity in determining the magnitude of speckle's effect is the number of independent speckle grains viewed by the receiver, which can be approximated as:

$$M \approx \frac{S_M}{S_c}, \quad \text{1)}$$

where S_M is the receiver area and S_c is the speckle correlation area [MacKerrow and Schmitt, 1997]. The speckle correlation area is given by:

$$\textbf{2)}\ S_c = \frac{\lambda^2 z^2}{\pi w_T{}^2},$$

where z is the distance between the target plane and the receiver plane and w_T is the laser spot size radius. Calculations using CATS nominal parameters show that a single observed beamlet footprint can be considered to be an integration of more than one thousand 'speckle grains' and thus the effects of speckle are considered negligible.

Because of the low signal levels expected at the receiver, quantum (shot) noise will have a significant impact on the number of detected photoelectrons. Poisson statistics describe the quantum noise in PMT detection under constant radiation field intensity [Liu, et. al, 1996]. The probability that there are n_t detected photoelectrons is given by:

$$\textbf{3)}\ P(n_t, n_s) = \frac{n_s{}^{n_t} \cdot e^{-n_s}}{n_t!},$$

where n_s is the expected number of photoelectrons. Figure 1 shows the probability of detecting at least one signal event given a single photoelectron threshold. With an expected signal of one photoelectron, there is a 36.8% probability that there will be no signal event registered.

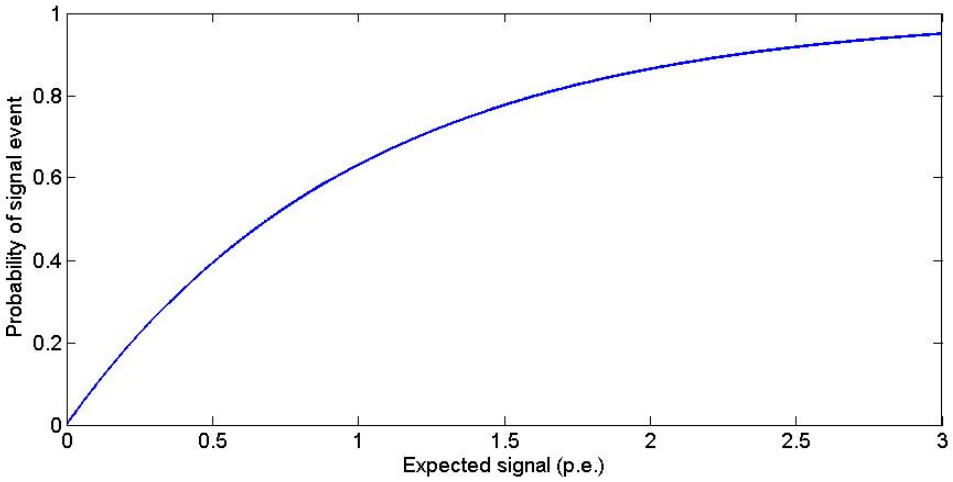

Figure 1: Probability of detecting at least one signal event (given a single photoelectron threshold) as a function of the expected signal strength in photoelectrons.

The normalized standard deviation of the Poisson process can be written as:

$$\textbf{4)}\ \overline{\sigma_{shot}} = \frac{1}{\sqrt{n_s}}$$

The high variance of the Poisson process at low signal levels requires careful consideration when implementing the discrete return waveform (Figure 2). Within individual range bins, the radiation field intensity is considered constant in order to generate the signal event realizations. Event realizations within each range bin are created through generation of exponentially-distributed time signatures, with distribution parameter based on the previously calculated

expected signal strength. This process is appropriate for our application because time intervals between occurrences of a Poisson process are described by an exponential distribution.

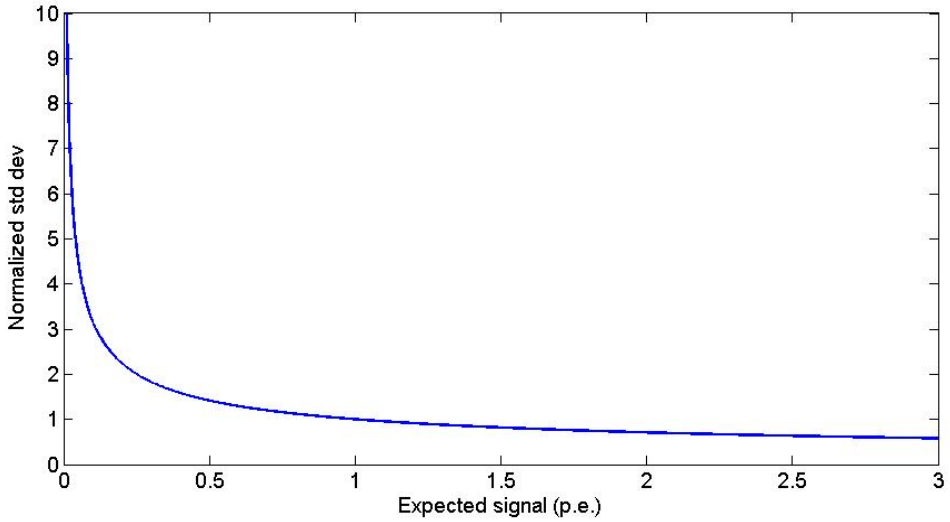

Figure 2: Normalized standard deviation of signal intensity due to shot noise.

Scintillation (variation in the irradiance intensity due to atmospheric turbulence) may be expected to have a significant effect on the return signal. For near-earth applications, the SLC Day Model can be used to estimate the refractive-index structure coefficient C^2_N [Beland, 1993]. Assuming a point detector and uniform distribution of turbulence, this estimation results in a value of 0.15 for the normalized standard deviation of intensity modulation due to scintillation along the 600-m one-way path [Hufnagel, 1978]. The two-way path contribution will be at most the square root of the sum of the squares of the one-way path contributions.

Taking into account the finite aperture of the system will reduce the deviation considerably due to an averaging effect. CATS parameters correspond to an aperture averaging factor of 0.05 or less, resulting in a final estimate of 0.01 for the normalized standard deviation [Fried, 1967]. It is therefore assumed that the contribution to irradiance fluctuation due to scintillation is trivial relative to that due to shot noise.

b) Ocean Environment Model

i) Environment Overview

Simulating returns from a coastal environment involves additional consideration for three primary signal components: returns from the ocean surface, returns from the water column, and returns from the ocean bottom. Ideally, a small portion of the incident beam is reflected from the surface (to aid in the determination of the mean sea elevation) while the remainder is refracted through the surface, traverses through the water column along a slant path, is diffusely reflected by the ocean bottom (or target), and travels back along the same optical path to the sensor [Guenther and Thomas, 1983]. This basic process is the core of the simulator's ocean environment model.

The ocean environment model as implemented here is not intended to provide an accurate shot-to-shot indicator of performance. The small footprints of LSNR laser altimeters encounter a

local ocean surface in which the statistics vary greatly from pulse to pulse, and a realistic approach to simulating this variability would necessarily involve creating a complex ocean realization with elements of centimeter scale, and tracing individual fractions of each incident beamlet through the medium. The approximate methods used in our model involve ensemble studies and statistical averages in order to provide an overall performance measure of entire test flights in a reasonable amount of computation time.

ii) Coastal Surface

Two aspects of the coastal ocean surface make significant contributions to the return waveform: diffuse reflection from oceanic whitecaps and specular glints from the wave structure. Algorithms detailing each aspect separately are described, followed by discussing on how the two processes are integrated into a functioning ocean surface model.

(1) Sea Foam

Oceanic whitecaps are typically assumed to be isotropic reflectors, allowing the straightforward application of the standard signal return equations to describe the returns from the surface sea foam. In general however, the effect of sea foam on shallow water bathymetry is not well-documented. For near-shore shallow waters, the equation for fractional coverage of the ocean surface by whitecaps as given by Monahan and MacNiocaill does not apply [E. C. Monahan and G. MacNiocaill, 1986]. Breaking waves in the surf zone induce a higher fractional coverage than that predicted for open ocean conditions. For this reason, the fractional coverage W has been designated a direct user input.

The reflectance of fresh dense sea foam has been studied in a laboratory setting to be ~55% [Whitlock, et. al, 1982]. This value is considered to be an overestimation when applied to a natural setting due to the fact that foam patches of different ages (and thus varying reflectances) will contribute to the return signal [Koepke, 1984]. The effective value of whitecap reflectance calculated by Koepke as 22% is a more realistic value given no previous knowledge of the foam age and is therefore used here.

(2) Wave influence

The ocean surface can be considered to be a “distorted mirror surface that gives rises to specular reflections or glints from wave facets that are aligned for backscattering to the laser receiver.”[Bufton, et. al, 1983] Wave slopes aligned perpendicular to the incident beam will therefore result in specular glints at the receiver.

The problem of estimating lidar backscatter from a randomly structured surface is exacerbated by the use of a small laser footprint. The probability density function of backscatter pulse energy has been shown to vary widely as a function of wind speed, incident angle, and a number of other environmental factors. Bufton’s derivation of the mean backscattered energy is therefore used as a simple representation of expected return signal. Using this ensemble value applied to each beamlet footprint will not result in the high variances seen in experimental data but will allow us to arrive at an average performance measure for the entire data set.

Our standard expression for signal strength can be adapted to backscatter from the sea surface by substituting ρ with an effective Lambertian reflectance, as defined by:

$$5)\ \rho_{eff} = \frac{r_{\text{int}} \sec^5(\alpha_s)}{4\langle S^2 \rangle} \exp\left(-\frac{\tan^2(\alpha_s)}{\langle S^2 \rangle} \right)$$

where r_{int} is the reflectance of the air-water interface, α_s is the angle of incidence on the mean ocean surface, and $\langle S^2 \rangle$ is the 2-D mean square wave slope [Bufton, et. al, 1983]. The reflectance of the air-water interface is described by Fresnel's equations for unpolarized incident radiant energy as:

$$6)\ r_{\text{int}} = \frac{1}{2}\left\{ \left[\frac{\sin(\alpha_s - \alpha_r)}{\sin(\alpha_s + \alpha_r)} \right]^2 + \left[\frac{\tan(\alpha_s - \alpha_r)}{\tan(\alpha_s + \alpha_r)} \right]^2 \right\},$$

where α_r is the refracted angle in the water medium as given by Snell's law. Although laser light is generally polarized, this formula serves as an approximation given the highly variable nature of the polarization vector over an entire lidar flight and the roughly equal polarization components at low incidence angle.

Simple expressions for the 2-D mean square wave slope in the open ocean as a function of wind speed have been developed by Cox and Munk, and Wu. These equations are not directly applicable to the surf zone but can be used as guidelines for assignment of wave slope values.

To estimate the centroid of the return signal from the wave structure, the expression for expected pulse delay developed by Tsai and Gardner is used [Tsai and Gardner, 1982].

$$7)\ T_s = \frac{2R_{air}}{c_{air}}\left(1+\tan^2(\gamma)\right) + \frac{2}{c_{air}\cos(\alpha_s)}\sigma_\eta \lambda_3 \left(1 - \frac{2\tan^2(\phi)}{\langle S^2 \rangle} \right),$$

where α_s is the incident angle on the mean sea surface. λ_3 is the sea surface skewness factor, with a value of 0 representative of a perfectly Gaussian distribution of sea waves. σ_η is the rms wave height.

Likewise, the expected mean square pulse width is given by:

$$8)\ \sigma_s^{\,2} = \sigma^2{}_h + \sigma^2{}_f + \frac{4\sigma_\eta^{\,2}}{c_{air}^{\,2}\cos^2(\alpha_s)}\left[1 - \lambda_3^{\,2}\left(\frac{1-2\tan^2(\alpha_s)}{S^2} \right)^2 \right] + \frac{4R^2}{c_{air}^{\,2}} \cdot \left(\tan^4(\gamma) + \tan^2(\gamma)\tan^2(\alpha_s) \right)$$

(3) Integrated Surface Model

For each beamlet footprint incident on the ocean surface, a uniform random variable is generated on the interval [0, 1]. This value is then compared to the fractional coverage parameter *W* to determine if the footprint is incident on sea foam. Foam is treated as a surface feature of infinitesimal thickness, and therefore absorption is not considered. For each footprint incident on a patch of sea foam, a portion of the incident energy is diffusely reflected while the remainder is transmitted through the foam. The specular reflection component from the wave structure is then computed, and the beam is propagated through the water column.

iii) Backscatter from the water column

As the laser propagates through the water column, there are two primary losses to consider: absorption and scattering. These losses are described by the spectral absorption and scattering coefficients $a(\lambda)$ and $b(\lambda)$, defined as the spectral absorptance and scatterance per unit distance in the medium. These values are known as inherent optical properties (IOPs); they depend only on the medium and are independent of the incident light field [Mobley, 1994].

Another useful quantity is the spectral volume scattering function, $\beta(\psi,\lambda)$, which is defined as the fraction of incident power scattered out of the beam at an angle ψ. ψ is known as the scattering angle and its value lies on the interval $0 \le \psi \le \pi$. Due to the small spot radius viewed by the receiver, single scattering will dominate the received signal and multiple scattering effects can be ignored [Gordon, 1982].

While IOP values generally vary with depth, we consider them constant since our expected system operation is over shallow waters (0 to 5 m deep). Although littoral zone waters often contain suspended sediment, in this work, any suspended sediment concentration is assumed vertically uniform because of the shallow depths.

Values for these functions can be taken from collected data or derived models. Values obtained for pure sea water and coastal waters are used in our simulations [Petzold, 1972].

All the losses of radiant power from a collimated beam of photons can be accounted for using the total beam attenuation coefficient $c(\lambda)$ [Mobley, 1994]. This quantity is described simply by:

$$\textbf{9)}\quad c(\lambda) = a(\lambda) + b(\lambda)$$

Wells proposed using a more realistic attenuation coefficient that allows for scattering within the receiver FOV [Wells, 1973]. Because of the small receiver aperture design in CATS, the signal contribution made by this addition is negligible. The simple attenuation coefficient calculated above is therefore fine for our purposes.

If all light scattered out of the collimated beam is considered lost and there to be no sources due to inelastic scatter or emission, a Beer's law approximation is appropriate to describe the attenuation of the light through the water column. Given initial energy E_0, the signal energy after traveling a distance R_w in the water medium is:

$$\textbf{10)}\quad E(R_w) = E_0 \exp(-c(\lambda)\cdot R_w)$$

The instantaneous expected backscatter energy (reaching the interface) from a distance R_w will be the energy backscattered from the beam multiplied by the transmission on the return trip to the interface.

$$\textbf{11)}\quad \begin{aligned} E_b(R_w) &= \left\{E(R_w)\cdot\beta(\pi)\cdot\Omega_r\right\}\cdot\exp(-c(\lambda)\cdot R_w) \\ &= E_0\cdot\beta(\pi)\cdot\Omega_r\cdot\exp(-2c(\lambda)\cdot R_w) \end{aligned}$$

Since $R_{air} >> R_w$, Ω_r is considered constant. After considering the two-way transmittance of the interface, propagation through the atmosphere, and efficiency characteristics, the expression for the expected signal (expected number of photoelectrons) from water column backscatter can be written as:

12) $$n_{s,col} = \eta_h \eta_q \eta_r \cdot \frac{E_t}{h\nu} \cdot \beta(\pi) \cdot \Omega \cdot \left[\frac{1 - \exp(-2c(\lambda) \cdot R_w)}{2c(\lambda)} \right] \cdot \left[1 - r_{\text{int}}(\alpha_s)\right]^2 \cdot \left[\exp(-\beta_e R_{air})\right]^2$$

The temporal spread of the water column signal is known (proportional to the beam intensity at depth) and therefore fitting the expected waveform to the range gate is straightforward.

iv) Returns from Ocean Bottom

Development of the expected signal strength from the ocean bottom closely resembles the process used in the air-only case. Terms for transmission loss through the air-water interface and through the water medium must be included, as well as adjustments to the beamlet direction vector to account for surface refraction. The previous expression for the Fresnel transmittance of the interface and the previous assumption of exponential decay of the beam through the water column are used to derive the signal intensity expression. Again assuming a purely Lambertian reflector, the equation for the expected number of photoelectrons generated by the ocean bottom signal is then:

13) $$n_{s,bottom} = \eta_h \eta_q \eta_r \cdot \frac{E_t}{h\nu} \cdot \rho \cos(\alpha_t) \cdot \frac{A_r}{\pi (R_{air} + R_w)^2} \cdot \left[1 - r_{\text{int}}(\alpha_s)\right]^2 \cdot \left[\exp(-\beta_e R_{air})\right]^2 \cdot \left[\exp(-c(\lambda) R_w)\right]^2$$

where α_t is the incident angle on the terrain (of the refracted daughter ray inside the medium).

To calculate the return pulse centroid delay and rms pulse width, the earlier expressions for air-water interface returns are modified to include terms for distortion due to the wave surface and geometric delay. Multipath time broadening is ignored due to the single scattering approximation. The signal waveform is then mapped to the range gate of the receiver electronics as before.

Development of the necessary adjustments to the noise model follow a similar process to the one detailed above, but will not be described explicitly. The distribution of noise events remains uniform and therefore implementation is straightforward.

c) Simulation Results

i) Topographic Simulation

A number of simulations have been run, under a variety of mission conditions. Because of the size limitations imposed on the progress report, a small sampling of results is presented here in order to demonstrate our ability to quantify system performance as a function of various parameters. A more complete report, including in-depth analysis, is available upon request.

The values for atmospheric and system parameters used are shown in Tables 1 and 2. The atmospheric parameters were chosen to simulate clear atmosphere. The system parameters were selected to represent a typical application of CATS. Unless otherwise noted, simulations were run at nadir view and at night-time, with a planar underlying virtual surface located at an elevation of 1 meter and with reflectance coefficient and surface profile variance of 0.3 and 0.01 m^2, respectively.

Table 1: Atmospheric parameters used for simulation.

Refractive Index	1.0003
Atmospheric Scale Height	1.2 km
Extinction Coefficient	.297e-3 / m

Table 2: System parameters used for simulation.

Platform Altitude	600 m
Receiver Channels	96
Pulse Frequency	8 kHz
Laser Beam Duration (FWHM)	480 ps
Laser Wavelength	532 nm
Transmitted Energy	3 μJ
Beamlet Divergence (half-angle)	.128 mrad
Inter-Beamlet Spread	.367 mrad
Hologram Efficiency	0.8
Telescope radius	0.033 m
Receiver IFOV	1.1e-5 sr
Bandpass filter	2.5e-10 m
Receiver Optical Efficiency	0.4
Detector Quantum Efficiency	0.28
Detector Dark Count	30e3 cps
Effective Dead Time	0.5 ns
Range Bin Length	0.5 ns
Range Gate Length	1 μs

Note that SNR as defined in our context is the number of recorded signal events to the number of recorded noise events. To estimate the SNR, the total number of events E and the total number of events in a window centered about the signal area E_S are first extracted from the elevation data. The window size must be chosen to be sufficiently large to include all possible signal returns accounting for pulse spread. Given the range gate duration τ_g and temporal window size τ_S, the intermediate quantity ζ is defined as:

$$\zeta = E_S - \left(\frac{\tau_S}{\tau_g - \tau_S} \right) \left(E - E_S \right) \quad \textbf{14)}$$

$\left(\frac{\tau_S}{\tau_g - \tau_S} \right)$ is the ratio of specified signal window size to the non-windowed portion of the range gate. SNR can then be estimated as:

$$SNR = \frac{\zeta}{E - \zeta} \quad \textbf{15)}$$

The total number of signal events can then be estimated as:

$$\textbf{16)}\ S = \frac{E \cdot SNR}{(1+SNR)}$$

Figure 3 is a logarithmic plot of the estimated SNR as a function of solar zenith angle as the surface reflectance is varied from 0.10 to 0.50. A practical application of LSNR lidar will encounter a variety of natural and/or artificial surfaces in a single data collection run. The corresponding reflectance values for these materials will vary widely.

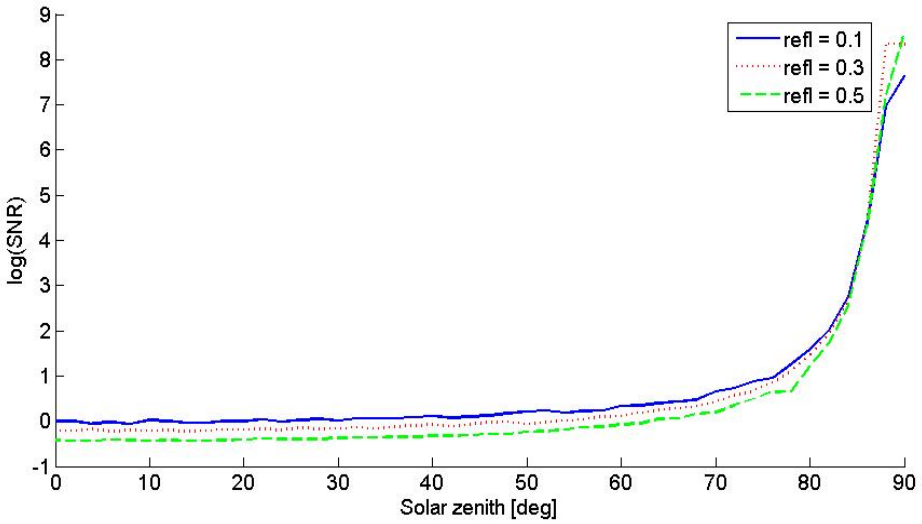

Figure 3: SNR plotted as a function of solar zenith angle. The surface reflectance coefficient was varied from 0.1 to 0.5.

Figure 4 further investigates SNR as the effective receiver dead time is varied from 0.1 ns to 2.0 ns. As the effective receiver dead time increases, the number of recorded signal returns is limited by pulse duration and signal spread effects. The effective receiver dead time of CATS has not been experimentally determined but will likely be limited by the rise/fall time of the PMT.

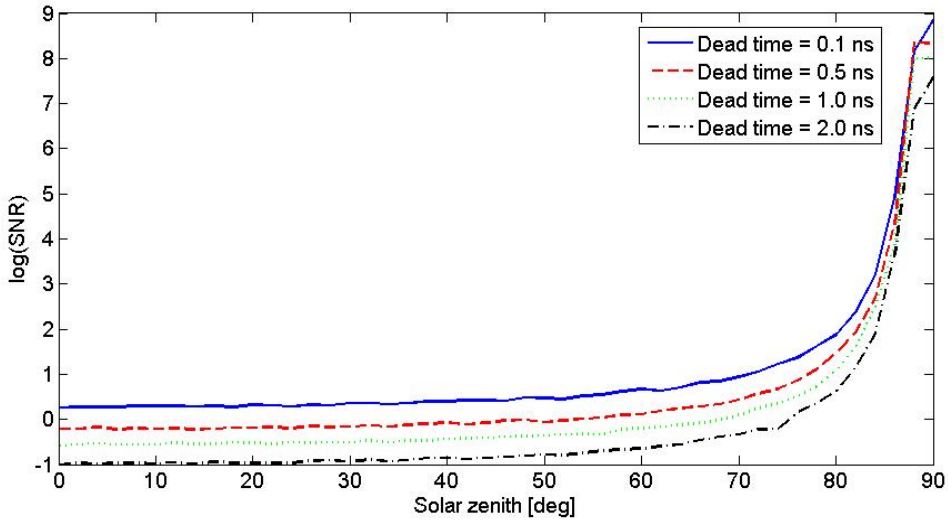

Figure 4: SNR plotted as a function of solar zenith angle. The effective receiver dead time was varied from .1 ns to 2 ns.

The mean and standard deviation of the number of signal events per beamlet footprint are valuable measures of signal strength and stability, and will not vary due to induced noise. Table 3 shows the mean number of signal events per beamlet footprint for various surface reflectance values.

Table 3: Mean and standard deviation of number of signal events detected per channel per footprint at nadir view, for various surface types.

Reflectance Coefficient	Mean signal events per channel	Standard Deviation
Surface Profile Variance = 0.00 m² (smooth)		
0.1	0.86	0.51
0.3	1.29	0.48
0.5	1.50	0.56
Surface Profile Variance = 0.01 m² (rough)		
0.1	1.15	0.80
0.3	2.27	0.84
0.5	2.89	0.80

Plotting the standard deviation of elevation values for every return event did not give us much meaningful information because of the spatial coherence of signal returns as compared to the sparse distribution of noise events throughout the range gate. Instead we chose to create a window about the expected terrain elevation and calculate the standard deviation of all events within this region. Window size is selected based on two criteria: 1) large enough to contain the entire signal region, allowing for pulse spread effects, and 2) small enough to avoid excessive noise counts. As there is no method to distinguish signal events from noise events within the

window, any noise events contained within the window will contribute to the standard deviation measurements. Figure 5 shows the standard deviation of elevation values in a +/- 1 m range window about the expected terrain elevation as a function of solar zenith angle.

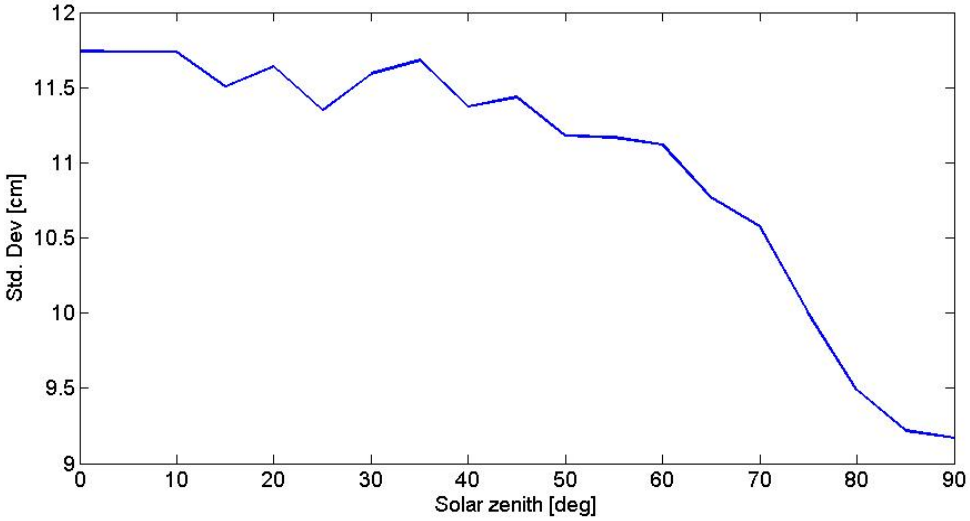

Figure 5: Standard deviation of elevation values in a 2 meter window centered about the true terrain. Observations were made at nadir view.

ii) Bathymetric Simulation

Bathymetric simulations were run for a variety of environmental conditions. Direct analysis of the initial output leads to erroneous results due to index of refraction effects, so further processing is required.

The following algorithm is used to correct elevation values from the sea bottom. An expectation maximization (EM) Gaussian mixture (GM) model first segments the sea surface from the bottom returns. Given the platform position and assuming a flat sea surface, the refracted daughter ray through the water medium is then computed. The underwater range component is adjusted for the sea water's index of refraction, and the new coordinate is projected from the intersection of the laser vector with the estimated sea surface.

Values for the IOPs obtained for natural clear water and coastal water are shown in Table 4 [Mobley, 1994]. Unless otherwise stated, simulation parameters are set as shown in Table 5.

Table 4: IOPs for bathymetric simulation.

		Value		
Parameter	**Symbol**	Pure Sea Water	Coastal Water	**Units**
Absorption coefficient	a	0.0517	0.179	1/m
Scattering coefficient	b	0.0025	0.219	1/m
VSF at 180°	$\beta(180°)$	2.94E-04	1.03E-03	1/m 1/sr

Table 5: Standard parameters for bathymetric simulation.

Parameter	Symbol	Value
Fractional foam coverage	W	0.10
Foam reflectance	ρ_foam	0.22
Skewness coefficient	λ_3	0.20
Mean Square Wave Slope	$\langle S^2 \rangle$	0.03
RMS wave height	σ_h	0.20
Bottom reflectance	ρ	0.30
Bottom surface profile variance	Var(ξ)	0.001
Solar zenith	θ_s	90°

Figure 6 shows histograms for bathymetric simulation over pure sea water, and Figure 7 shows similar results for simulation over coastal waters. Sea depths of 2 m and 5 m were used. Note that an artifact appears in the water column portion of the histograms due to the corrected projection of points below the EM GM decision boundary. There is significant overlap between elevation values of corrected and non-corrected points in the water column, resulting in a higher than expected number of counts near the EM GM threshold; this phenomenon can be ignored as the uncorrected histograms display the expected exponential form for the water column backscatter.

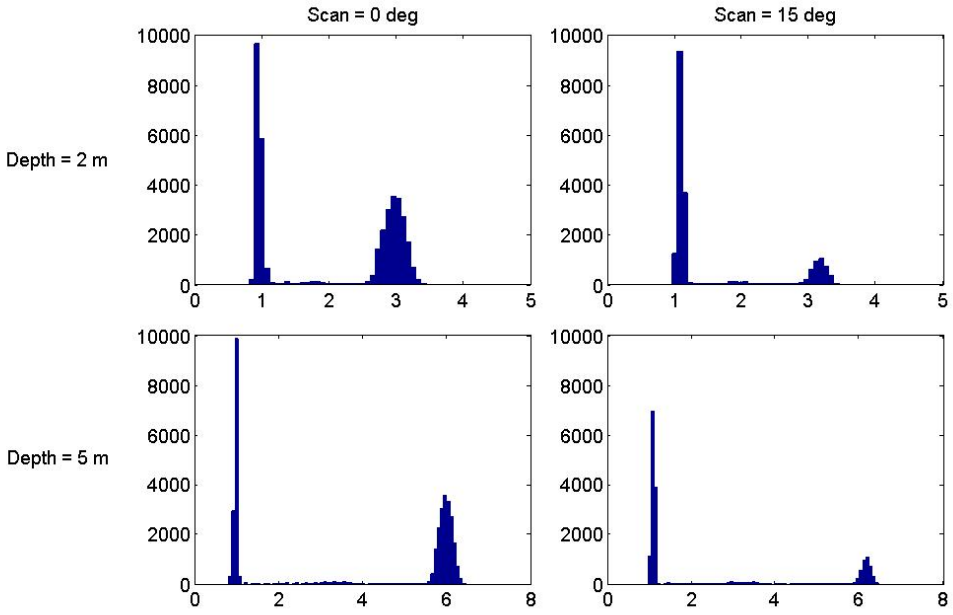

Figure 6: Elevation histograms for 100 simulated footprints over pure sea water.

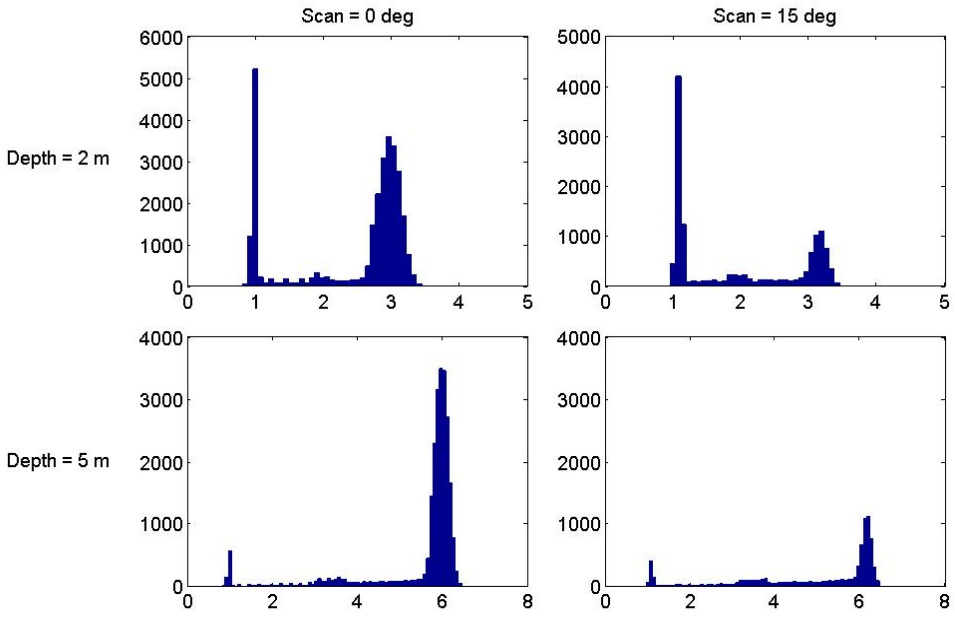

Figure 7: Elevation histograms for 100 simulated footprints over coastal ocean conditions.

The dependence of system performance on sea surface conditions was investigated by varying the foam fractional coverage from 0% to 60% in 20% increments. The resulting number of recorded signal events is shown in Table 6. Simulation was run using coastal ocean parameters, with a sea depth of 2 m. For nadir view, the number of recorded signal events decreased by approximately 14% as fractional foam coverage increased to 60%. For the scanner extrema, the decrease was 22%.

Table 6: Mean number of recorded signal events per beamlet for a sea depth of 2 m in coastal conditions. Foam coverage is varied from 0% to 60%.

	Mean # of Signal Events	
Foam Coverage	Scan = 0°	Scan = 15°
0%	0.71	0.63
20%	0.66	0.57
40%	0.62	0.54
60%	0.56	0.49

Bathymetric performance was also evaluated for a range of bottom reflectance coefficients. The results are shown in Table 7.

Table 7: Mean number of recorded signal events per beamlet for a sea depth of 2 m in coastal conditions. Reflectance coefficient is varied from 0.1 to 0.4.

	Mean # of Signal Events	
Reflectance Coefficient	Scan = 0°	Scan = 15°
0.1	0.27	0.24
0.2	0.49	0.43
0.3	0.67	0.61
0.4	0.85	0.75

Future Work

The question of data filtering and segmentation in a low SNR system has only been given minimal attention thus far in our work. Data sets obtained from LSNR ALSM systems will include far more noise events than data sets from traditional ALSM systems. For filtering purposes, the high spatial coherence of signal events implies application of a spatial coherence algorithm like the Correlation Range Receiver [Degnan, 2001], which has thus far demonstrated good preliminary performance. We intend to investigate improvements to this algorithm specific to our lidar application.

An interesting application of low SNR systems is in the detection of small targets, both in dry-earth and littoral scenarios. While the high resolution of data points in LSNR lidar leans towards the ability to detect sub-1 meter targets, the strength of returns may limit the probability of detection in some scenarios (deep, turbid waters for example). We plan on evaluating target detection performance for a variety of simulator inputs and detection algorithms.

The ability to penetrate canopy and map the forest floor has been demonstrated for small footprint lidar systems. A multiple return, multiple beamlet LSNR lidar system should provide superior mapping of the vegetated zone. This performance advantage will be evaluated through implementation of an improved canopy model. A preliminary model has been presented to David Harding and will be improved to include realistic forestry characteristics.

We intend to correspond regularly with NASA Goddard personnel to ensure that other goals, such as outlining my PhD dissertation topic, are consistent with NASA interests. In particular, Dr. Slatton and I will coordinate with Dr. David Harding at NASA Goddard (the technical point of contact for my NASA GSRP Fellowship). We have already had discussions with him, and a presentation of work thus far was made to Dr. Harding in early fall 2007 and received his approval.

References

A. I. Borisenko and I. E. Tarapov, *Vector and Tensor Analysis with Applications*, Dover, 1968.

B. M. Tsai and C. S. Gardner, "Remote sensing of sea state using laser altimeters," *Applied Optics*, vol. 21, pp. 3932-3940, 1982.

C. Cox and W. Munk, "Measurements of the roughness of the sea surface from the sun's glitter," *J. Opt. Soc. Am.*, 1954.

C. H. Whitlock, D. S. Bartlett and E. A. Gurganus, "Sea Foam Reflectance and Influence on Optimum Wavelength for Remote Sensing of Ocean Aerosols," *Geophys. Res. Lett.*, vol. 9, p. 719, 1982.

C. Mobley, *Light and Water: Radiative Transfer in Natural Waters*, Academic Press Inc., 1994

D. L. Fried, "Aperture Averaging of Scintillation," *Journal of the Optical Society of America*, vol. 57, no. 2, 1967.

E. C. Monahan and G. MacNiocaill, "Whitecaps and the passive remote sensing of the ocean surface," *Int. J. Remote Sensing*, vol. 7, pp. 627-642, 1986.

E. P. MacKerrow and M. J. Schmitt, "Measurement of integrated speckle statistics for CO2 lidar returns from a moving, nonuniform, hard target," *Applied Optics*, Vol. 36, No. 27, pp. 6921-6937, 1997.

G. Guenther and R. Thomas, "System design and performance factors for airborne laser hydrography," *OCEANS*, vol. 15, pp. 425-430, 1983.

G. Fuller, *Analytic Geometry*, 5th ed., Addison Wesley, 1980.

H. R. Gordon, "Interpretation of airborne oceanic lidar: effects of multiple scattering," *Applied Optics*, vol. 21, pp. 2996-3001, 1982.

J. J. Degnan, McGarry, T. Zagwodzki, P. Dabney, J. Geiger, R. Chabot, C. Steggerda, J. Marzouk, and A. Chu, "Design and Performance of an Airborne Multikilohertz Photon-counting, Microlaser Altimeter," *Proceedings of Land Surface Mapping and Characterization Using Laser Altimetry*, Vol. XXXIV3-W4 International Archives of Photogrammetry and Remote Sensing, Annapolis, MD, pp. 9-16, Oct22-24, 2001.

J. L. Bufton, F. E. Hoge, and R. N. Swift, "Airborne measurements of laser backscatter from the ocean surface,"*Applied Optics*, vol. 22, pp. 2603-2618, 1983.

J. W. Goodman, "Statistical Properties of Laser Speckle Patterns," in *Laser Speckle and Related Phenomenon*, J. C. Dainty, Ed., Springer-Verlag, 1975.

J. Wu, *Phys Fluids*, vol. 5, p. 741, 1972.

K. Clint Slatton, William Carter, and Ramesh Shrestha, "A Simulator for Airborne Laser Swath Mapping via Photon Counting," *Proc. SPIE Defense and Security Symposium*, vol. 5794, Mar. 2005, pp. 12-20.

P. Koepke, "Effective reflectance of oceanic whitecaps," *Applied Optics*, vol. 23, pp. 1816-1824, 1984.

R. E. Hufnagel, "Propagation Through Atmospheric Turbulence," in *The Infrared Handbook*, W. L. Wolfe and G. J. Zissis, Eds. (U.S. GPO, Washington D.C., 1978), Chap 6.

R. R. Beland, "Propagation through atmospheric optical turbulence," in *The Infrared and Electro-Optical Systems Handbook*, F. G. Smith, Ed. (SPIE Optical Engineering Press, Bellinghan, WA, 1993), vol. 2. ch 2.

T. J. Petzold, "Volume scattering functions for selected ocean waters," SIO Ref. 72-78, Scripps Inst. Oceanogr., LaJolla, 79 pp, 1972.

W. E. Carter, R. L. Shrestha, and K. C. Slatton, "Photon Counting Airborne Laser Swath Mapping (PC-ALSM)," *IAG International Association of Geodesy Symposia: Gravity, Geoid and Space Missions (GGSM)*, invited, Aug., 2004, vol. 129, pp. 214-217.

W. H. Wells, "Theory of small angle scattering, " *NATO Publication AGARD-LS-61*, 1973.

Z. Liu, W. Hunt, M. Vaughan, C. Hostetler, M. McGill, K. Powell, D. Winker, and Y. Hu, "Estimating random errors due to shot noise in backscatter lidar observations," *Applied Optics*, vol. 45, pp. 4437-4447, 2006.